7

On the Applicability of Photonic Crystal Membranes to Multi-Channel Propagation

Bartłomiej Salski[1], Kamila Leśniewska-Matys[1] and Paweł Szczepański[1,2]
[1]*Warsaw University of Technology*
[2]*National Institute of Telecommunications*
Poland

1. Introduction

The most common 2D geometrical arrangements of photonic crystals (PhC) are square and triangular (hexagonal) lattices as shown in Fig.1. Assuming that a PhC structure is expanded to infinity along the x-axis, the problem belongs to a so-called vector 2D class (Gwarek et al., 1993). However, it may frequently be simplified even further to a scalar 2D class, restricting a wave vector *k* to a PhC plane (yz-plane in Fig.1). In such a case, any electromagnetic field propagating in the PhC plane can be decomposed into two orthogonal modes, usually denoted as transverse magnetic (TM) and transverse electric (TE) with respect to the x-axis.

Although performance of PhC-based devices relies, in most cases, on the confinement of light within a photonic bandgap (PBG), photonic crystals also exhibit remarkable dispersion properties in their transmission bands, thus opening the perspective for new optical functionalities.

A lot of research activities have been undertaken in the development of planar PhC passive optical devices, like waveguides (Loncar et al., 2000; Chow et al., 2001), filters (Ren et al., 2006; Fan et al., 1998), couplers (Yamamoto et al., 2005; Tanaka et al., 2005), power splitters (Park et al., 2004; Liu et al., 2004) or, recently, active devices for laser beam generation operating as a surface-emitting microcavity laser (Srinivasan et al., 2004), a photonic band-edge laser (Vecchi et al., 2007) or an edge-emitting laser (Shih et al., 2006; Lu et al., 2009). However, PhC devices in practical realizations are of a finite thickness (see Fig.2), thus, limiting applicability of the approximate 2D modelling approach to those scenarios where the PhC's thickness is large enough with respect to wavelength. Otherwise, the problem becomes 3D and a complete full-wave EM approach is essential.

Similarly to 2D waveguiding slabs, optical confinement of light in thin membranes depends primarily on a contrast between the membrane's and cladding's refractive indices. Most of all, a propagating mode has to be located beyond a light cone of the cladding, if energy leakage wants to be suppressed. Secondly, the mode has to be confined within a channel processed between the surrounding photonic crystal boundaries. The photonic bandgap exists only for those modes that are totally internally reflected at the interface between the channel and the photonic crystal. Furthermore, if the membrane is deposited on a low-index dielectric film, instead of being symmetrically surrounded with air, additional complications of a design process are introduced.

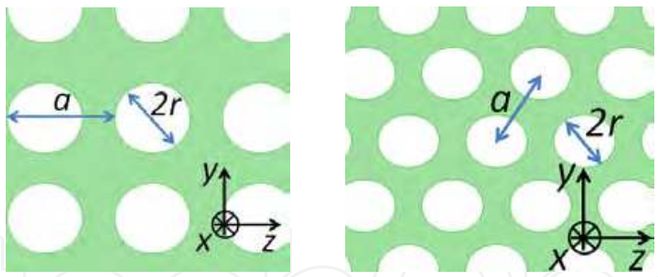

Fig. 1. The definition of square (left) and triangular (right) air-hole lattices.

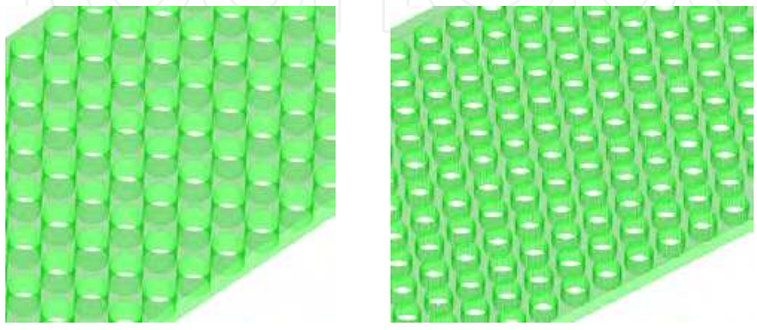

Fig. 2. A perspective view of dielectric membranes with square (left) and triangular (right) PhC air-hole lattices.

In the next Section, a brief overview of the developments of mutli-channel laser generation techniques is given, especially in the context of so-called supermode multi-channel propagation.

2. State-of-the-art in multi-channel laser generation techniques

A phase-locked operation of multi-channel waveguide devices supporting propagation of lateral modes (also known as supermodes) was studied mostly in 80's. The main goal of theoretical and experimental research was to achieve higher power density of the coherent laser beams generated in semiconductors. Phased array lasers, consisting of *N* single-mode waveguides, can guide, in total, *N* array modes. In practice, the most likely excited mode is of the highest order (Yariv, 1997). Consequently, relatively broad far-field patterns as well as broad spectral linewidths are obtained. To solve or at least alleviate that disadvantageous property, it is essential to distinguish appropriate supermodes.

Fig.3 shows near-field patterns of five supermodes supported by index-guided arrays consisting of five identical and non-identical channels. The supermode patterns were calculated with a numerical solver of Maxwell's equations (Kapon et al., 1984a). In particular, the excitation of a fundamental supermode results in a single-lobe radiation beam aligned with the array channels. However, as it has been shown in Fig.3a, in uniform arrays with identical channels, intensity patterns of the fundamental and the highest order supermodes are similar to each other, so their discrimination becomes difficult. Moreover, as it has been shown in (Kapon et al., 1984a), since inter-channel regions are usually lossy, the highest order supermode, with a two-lobe far field pattern, is often favoured over the other modes. Subsequently, variation in the channels' width (known as chirped arrays)

results in significantly different near field envelope patterns of the fundamental and higher-order supermodes, in contrast to the case of uniform arrays (Kapon et al., 1984a). In such arrays, higher order supermodes can be suppressed by employing a proper gain distribution.

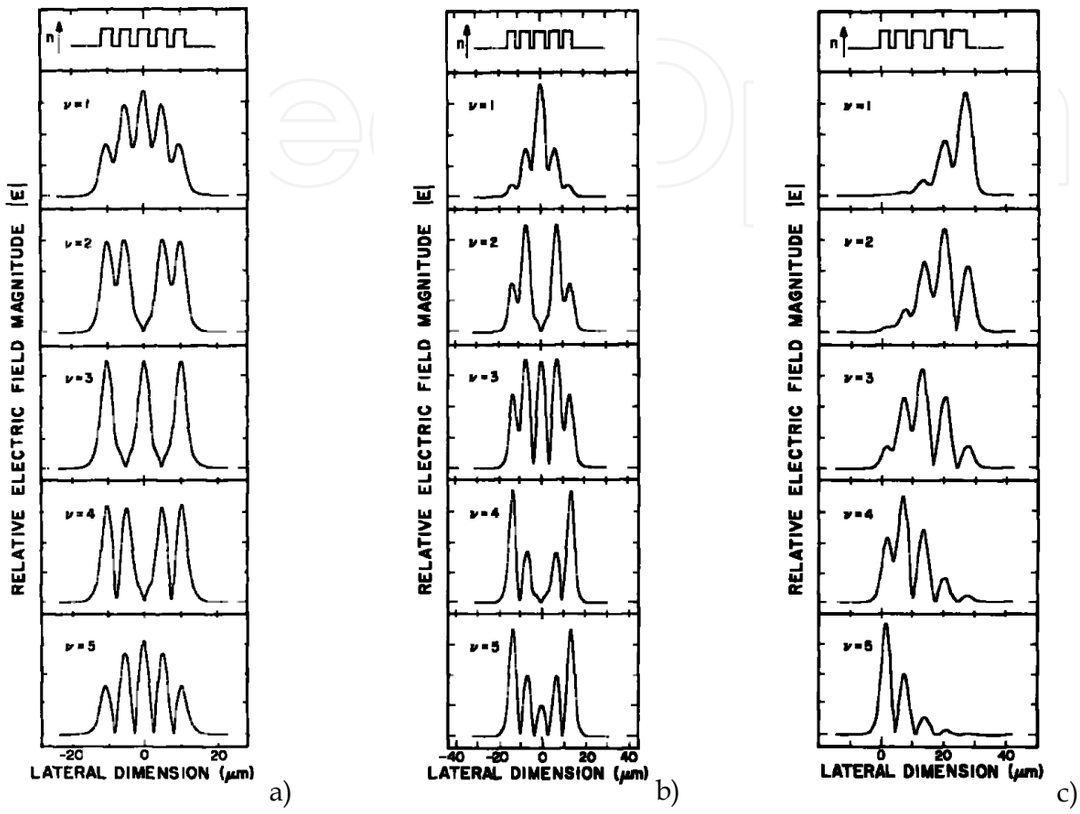

Fig. 3. Near-field patterns of the supermodes in a five-element a) uniform array b) inverted-V chirped array, c) linearly chirped array (Kapon et al., 1984a).

Next, in an inverted-V chirped array (Fig.3b), the power of the fundamental supermode is concentrated in central channels, whereas the higher order supermodes are more localized in the outermost channels. Since gain in the active region is larger when the laser channels are wider, the fundamental supermode is expected to have a higher modal gain (near threshold) and, in consequence, is more likely to oscillate (Kapon et al., 1984b).

In (Kapon et al., 1986), a buried ridge array has been proposed. In such arrays, a small refractive index contrast between the channels and inter-channel regions is applied. That soft index profile ensures effective coupling between the adjacent array laser channels via their evanescent optical fields. Since the channels in those arrays are defined by a built-in distribution of the refractive index, it is possible to achieve a uniform gain distribution across the array, while maintaining the channel definition. Such an approach makes the buried ridge arrays different from the gain guided arrays, in which inter-channel regions are inherently more lossy. Moreover, buried ridge arrays operate mainly with the fundamental supermode, thus, producing a single-lobe radiation beam.

The first analytical interpretation of supermodes behaviour in the phased array lasers was proposed in (Scifres et al., 1979). Experimental data was interpreted by considering a diffraction pattern of a structure with equally-spaced slits corresponding to individual laser array elements. Such an approach is usually known as a simple diffraction theory. Although the simple diffraction theory has been proved useful to interpret some experimental results (Scifres et al., 1979; AcMey & Engelmann, 1981; van der Ziel et al., 1984), it provides no means to describe the allowed oscillating modes in the array of coupled emitters.

In the early 70's, an alternative method, known as a coupled mode theory, was intensively investigated (Yariv, 1973; Yariv & Taylor, 1981; Kogelnik, 1979). It has been successfully applied to the modelling and analysis of various guided-wave optoelectronic and fibre optical devices, such as optical directional couplers (Taylor, 1973; Kogelnik & Schmidt, 1976), optical fibres (Digonnet & Shaw, 1982; Zhang & Garmire, 1987), phase-locked laser arrays (Kapon et al., 1984c; Mukai et al., 1984; Hardy et al., 1988), distributed feedback lasers (Kogelnik & Shank, 1972) and distributed Bragg reflectors (Schmidt et al., 1974).

One of major assumptions made in the conventional coupled mode theory is that the modes of uncoupled systems are orthogonal to each other. In coupled systems, however, one often chooses the modes of isolated systems as the basis for the mode expansion and these modes may not be orthogonal. Therefore, the orthogonal coupled mode theory (OCMT) is not suitable for the description of the mode-coupling process in that case. Non-orthogonality of modes in optical couplers, due to crosstalk between the waveguide modes, was first recognized in (Chen & Wang, 1984). Later on, several formulations of the non-orthogonal coupled mode theory (NCMT) were developed by several authors (Hardy & Streifer, 1985; Chuang, 1987a; Chuang, 1987b; Chuang, 1987c). It has been shown that NCMT yields more accurate dispersion characteristics and field patterns for the modes in the coupled waveguides. Better accuracy is even more essential to the modelling of coupling between non-identical waveguides. It is evident for weak coupling, though the new formulation extends the applicability of the coupled mode theory to geometries with more strongly coupled waveguides. However, NCMT becomes inaccurate when considering very strongly coupled waveguide modes (Hardy & Streifer, 1985).

To the best of authors' knowledge, edge-emitting multi-channel membrane lasers have not been manufactured so far, although single-channel membrane lasers processed on a GaAs photonic crystal membrane were already presented (Yang, et al., 2005; Yang, et al., 2007; Lu, et al. 2009). One of the major reasons lies in technological challenges in achieving acceptable repeatability of the photonic crystal structure manufacturing process (Massaro, et al., 2008). However, with the advent of new technology nodes those challenges will likely be overcome or at least substantially alleviated, opening a wide range of applications to the methodology addressed below.

In this Chapter, a complete design cycle of a new type of phased array laser structures processed in photonic crystal membranes is presented. Due to a very strong coupling between the adjacent channels in the array, a non-orthogonal coupled mode theory was applied in order to maintain the rigidity of the analysis.

3. Numerical modelling of optical channels in photonic crystal membranes

A complete electromagnetic design cycle of single- and multi-channel optical propagation in PhC membranes is presented in this Section, together with the computational methods and

tools applied. First, dispersive properties of an infinitely large PhC membrane with no defects are investigated to exemplify general rules for the photonic bandgap (PBG) generation as a function of PhC membrane geometry and incident light wavelength. Once a PBG dispersion diagram is achieved, a defect channel is processed in the PhC membrane and dispersive properties of such an optical waveguide are considered. For the purpose of this Chapter, propagation of transverse–electric (TE) modes in defect PhC membrane channels based on the square lattice type is studied only. However, the introduced methodology may be easily extended to other lattice types with either TE or TM polarisation. The obtained PBG diagrams will help detecting the supermodes within a photonic bandgap. Eventually, electric field patterns of those modes are computed to assess their applicability to the laser beam generation. As it is shown in Section 4.3, those field distributions are useful to calculate laser characteristics of the single- and multi-channel photonic crystal membrane lasers.

3.1 Bandgaps in photonic crystal membranes

Two common lattice types processed in a photonic crystal membrane are investigated, namely square and triangular (see Fig.4). The lattices are cut with air holes in an indium gallium arsenide phosphide (InGaAsP) layer with a refractive index of n = 3.4. At this stage, the goal is to specify design rules for the photonic bandgap generation as a function of the most critical parameters of those structures, that is, a membrane's thickness d, a lattice constant a and an air holes' radius r.

Numerical computations are performed using a full-wave electromagnetic approach with a finite-difference time-domain (FDTD) method implemented in a QuickWave-3D simulator (Taflove & Hagness, 2005; QWED). Since the structure is periodic in two dimensions, the computation with FDTD is enhanced with the Floquet's theorem (Collin, 1960), also known as the Bloch's one, which allows us to reduce a computational domain to a single period of the lattice (Salski, 2010), as exemplified in Fig.4. Considering periodicity along the z-axis, the following periodic boundary conditions (PBCs), derived from the Floquet's theorem, are enforced at periodic faces of the structure:

$$\vec{E}_{\perp}(x,y,z+L,t) = \vec{E}_{\perp}(x,y,z,t)\, e^{j\psi} \tag{1}$$

$$\vec{H}_{\perp}(x,y,z,t) = \vec{H}_{\perp}(x,y,z+L,t)\, e^{-j\psi} \tag{2}$$

where L is the period of the structure along the z-axis, $\perp$ denotes the components transverse to periodicity (in this case x- and y- components), and ψ is a fundamental Floquet phase shift per period L understood as a user-defined parameter.

As it has been shown in (Celuch-Marcysiak & Gwarek, 1995; Salski, 2010), incorporation of the Floquet's theorem into FDTD schemes results in a complex notation of time-domain electromagnetic fields with the real and imaginary FDTD grids computed simultaneously at the same structure's mesh and coupled via PBCs in each iteration cycle. The method is known as Complex-Looped FDTD (CL-FDTD) and is implemented in the QuickWave-3D simulator (QWED). Additionally, due to conformal meshing implemented in QuickWave-3D (Gwarek, 1985), curvature of the air holes, as shown in Fig.4, is accurately represented on

the FDTD mesh with no deteriorating effect on memory storage and computing time. A vertical cross-section of a unit membrane lattice cell sketched in Fig.4 (right) indicates that the structure is situated in air which, in order to reduce the computational volume, is truncated with absorbing boundary conditions, usually known as Mur superabsorption (Mei et al., 1992).

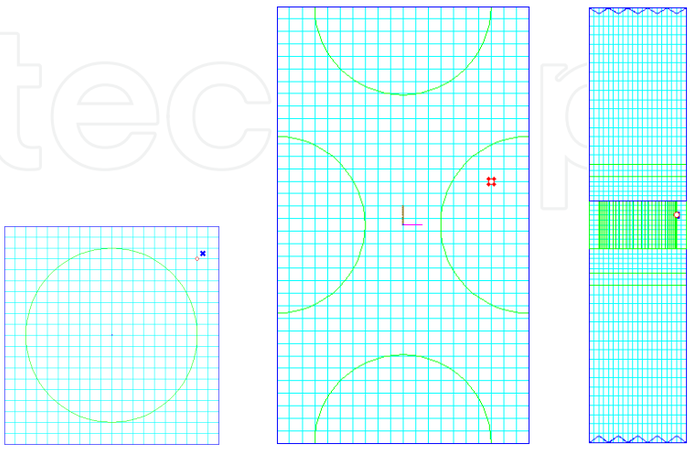

Fig. 4. A horizontal cross-section view of FDTD models of a unit cell of square (left) and triangular (centre) air-hole lattices and a vertical cross-section (right) with absorbing boundary conditions truncating the air regions below and above the membrane.

In each simulation run, for a particular set of Floquet's phase shifts per y- and z- periods, a point excitation located somewhere inside a unit cell is driven with a wideband pulse (e.g. a Dirac's delta), injecting energy into the structure. As the simulation continues, the Fourier transform is iteratively calculated until a convergent state is achieved. Fig.5 shows an exemplary spectrum of an injected electric current for the lattice shown in Fig.4 (left). Resonances indicate the eigenvalues (frequencies) of the detected modes satisfying Floquet's phase shifts imposed by periodic boundary conditions.

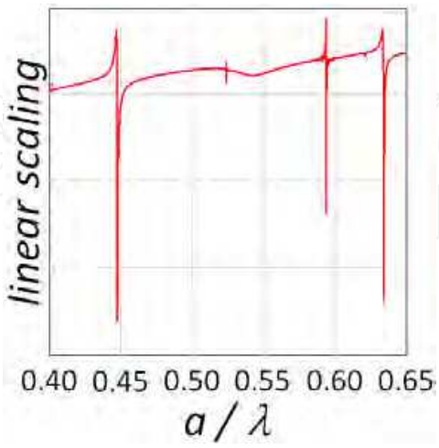

Fig. 5. The spectrum of an electric current injected into a unit cell of a square PhC membrane as shown in Fig.4 (left) with the imposed Floquet's phase shifts along y- and z-axis $\psi_y = \psi_z = 0$ radians ($n = 3.4$, $r/a = 0.4$, $d/a = 0.4$).

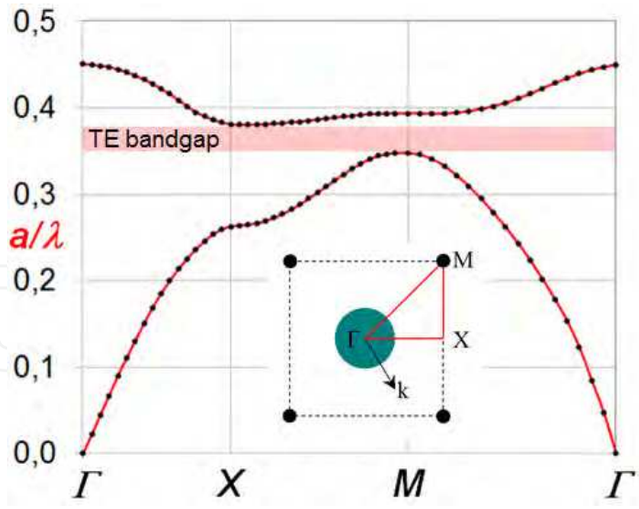

Fig. 6. A TE mode photonic bandgap diagram for an air-hole square lattice cut in an InGaAsP membrane (n = 3.4, r/a = 0.4, d/a = 0.4).

Owing to the wideband spectral properties of the CL-FDTD method, a single simulation provides information about all the modal frequencies within the spectrum of our interest satisfying the imposed Floquet's phase shifts. Thus, the simulator has to be invoked as many times as the number of wave vector points chosen to collect a PBG diagram along a whole contour of an irreducible Brillouin zone (Salski, 2010). In this case, a single simulation of the model consisting of 18 400 FDTD cells (ca. 4MB RAM) takes 11 seconds on Intel Core i7 CPU 950 with the speed of 1785 iter/sec. An FDTD cell size is set to $a/20$, leading to at least 40 FDTD cells per wavelength in free space and ca. 12 in the membrane. Calculation of the whole PBG diagram shown in Fig.6 with 55 wave vector points takes, in total, ca. 55 x 11 sec = 10 minutes.

In the case of an air-hole square lattice cut in an InGaAsP membrane, the PBG diagram of which is shown in Fig.6, an 8.8% wide indirect *X*-*M* TE bandgap for the normalised frequency a/λ = 0.348 … 0.380 is found. Although it is not exemplified in Fig.6, a TM bandgap is not present in that spectrum range, what may be considered as a potential disadvantage in applications when the precise control of beam propagation is necessary. It can be solved using a triangular lattice, where both TE and TM bandgaps may coincide within the same spectrum range. However, this issue extends beyond the scope of the Chapter and is not considered here.

Consider now the impact of geometrical settings on a TE bandgap in the investigated square PhC membrane. Fig.7 shows the modal dispersion as a function of the membrane's thickness d/a. It can be seen that, the TE bandgap decreases with the increasing membrane's thickness d/a, while covering the spectrum width of 8.8%, 9.2% and 10.4% for d/a = 0.4, 0.5 and 0.6, respectively. It shows that the membrane's thickness d/a has a relatively minor impact on the photonic bandgap width. Next, Fig.8 presents the computation results for a variable air-holes' radius r/a, and it is evident that the radius, in contrast to the membrane's thickness, has a substantial impact on the bandgap width, which reaches zero below ca. r/a = 0.25. Later in this paper, those PhC structures are applied for single- and multi-channel propagation of optical pulses.

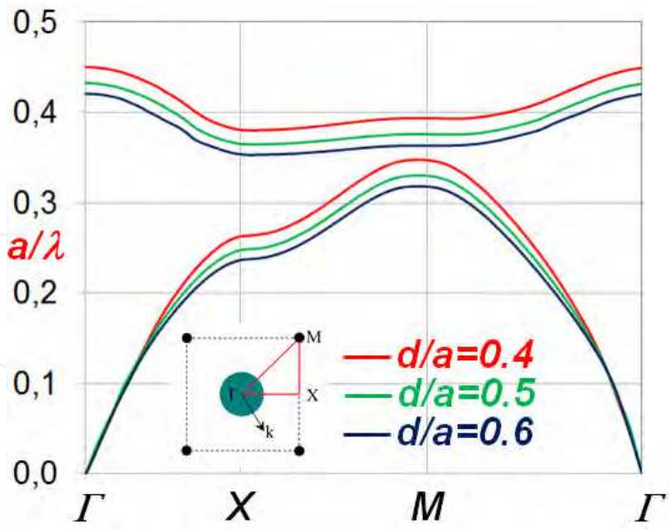

Fig. 7. TE mode photonic bandgap diagrams for air-hole square lattices cut in an InGaAsP membrane in function of a membrane's thickness d/a (n = 3.4, r/a = 0.4).

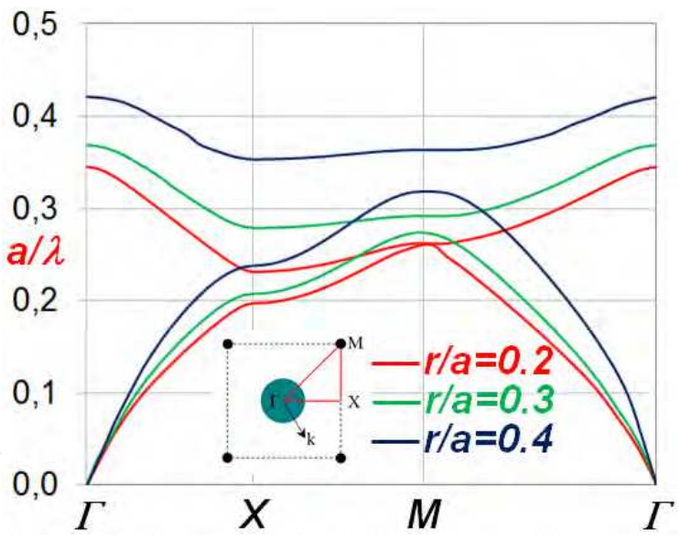

Fig. 8. TE mode photonic bandgap diagrams for air-hole square lattices cut in an InGaAsP membrane in function of an air-holes' radius r/a (n = 3.4, d/a = 0.4).

Similar computations were carried out for a membrane with a triangular air-hole lattice. First of all, as it may be inferred from Fig.9, a direct TE bandgap is achieved at a Γ critical point. Secondly, the achieved TE bandgap spectra are much wider when compared to their counterparts computed for the square lattice. Fig.9 shows that the spectrum width amounts to 40.7%, 42.6% and 43.8% for d/a = 0.4, 0.5 and 0.6, respectively. Next, Fig.10 depicts the impact of the air-holes' radius r/a on the TE bandgap spectrum width, which amounts to 16.6%, 40.7% and 36.9% for r/a = 0.3, 0.35 and 0.4, respectively. The simulations show that if a narrow bandgap is favourable in a considered application, the square lattice is a better option, while the triangular one allows creation of a wider bandgap.

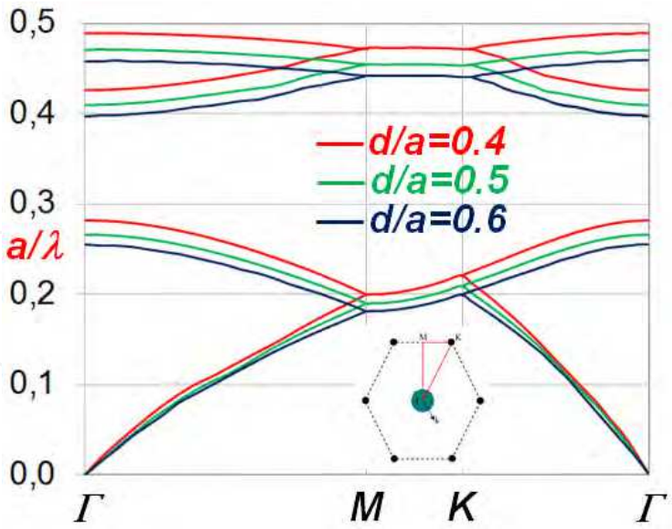

Fig. 9. TE mode photonic bandgap diagrams for air-hole triangular lattices cut in an InGaAsP membrane in function of a membrane's thickness d/a (n = 3.4, r/a = 0.35).

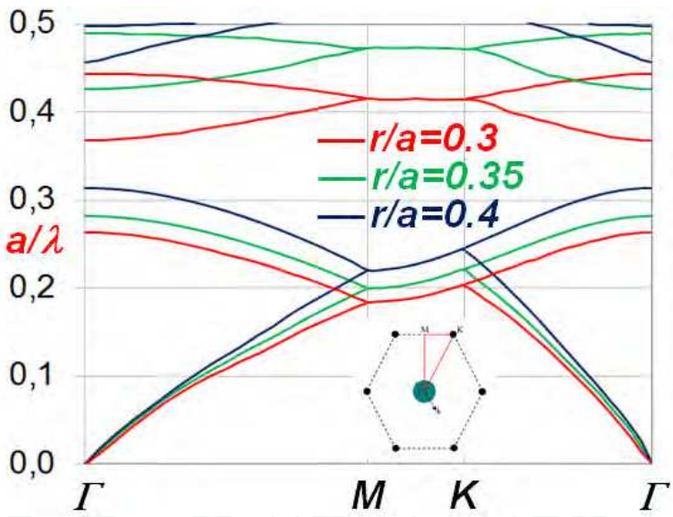

Fig. 10. TE mode photonic bandgap diagrams for air-hole triangular lattices cut in an InGaAsP membrane in function of an air-holes' radius r/a (n = 3.4, d/a = 0.4).

Concluding, it may be noticed from the investigation given in this Section and from the literature as well, that two-dimensional air-hole photonic crystals processed in thin dielectric membranes exhibit the following properties:

- PBG for TE modes shifts up in frequency and broadens with the increasing air-holes' radius r/a for both square and triangular air-hole lattices,
- PBG for TE modes shifts up in frequency with the increasing membrane's thickness d/a with no meaningful influence on its bandwidth for both square and triangular air-hole lattices,
- a PBG bandwidth for TE modes is much wider when a triangular air-hole lattice is used,

- PBG cannot be created for TM modes in a two-dimensional square air-hole photonic crystal processed in a dielectric membrane, while it is feasible in a triangular one when the membrane is thick enough (Joannopoulos et al., 2008).

3.2 Bandgaps in defect channels processed in photonic crystal membranes

Spectral properties of TE modes propagating in defect channels, as exemplified in Fig.11, processed in PhC membranes are investigated below. PBG diagrams are computed with the aid of the QuickWave-3D electromagnetic FDTD simulator (QWED), in the same way as in the case of non-defect PhC membranes as shown in Fig.4. This time, however, an FDTD model consists of a single PhC row, as marked with a red dashed line in Fig.11. Since it is assumed that the waveguide is infinitely long, the Floquet's periodic boundary conditions are enforced only along the channel's axis, while lateral dimensions are truncated with the absorbing boundary conditions (Mei, 1992). PBG diagrams for the square lattice channels are computed for phase shifts within a range designated by Γ and X critical points of the first irreducible Brillouin zone of the corresponding non-defect PhC membranes.

Fig.12 depicts the modes computed for a single square channel in an air-hole square lattice cut in an InGaAsP membrane (n = 3.4, r/a = 0.4, d/a = 0.4, b/a = 0.3). Black curves indicate the propagating modes with one distinguished by a green colour, while the red curves depict the modes of the non-defect PhC membrane surrounding the channel. It can be seen that a single defect mode is achieved (green) within a photonic bandgap (red semi-transparent zone) of the surrounding PhC. The mode has a uniquely defined phase constant within the a/λ = 0.356… 0.369 spectrum range, that is 3.6% wide, although a light cone additionally limits the allowed spectrum range to a/λ = 0.356… 0.365 (2.5% wide). Since single-mode propagation is achievable in that spectral range, it may be useful to design edge-emitting lasers based on 2D photonic crystal membranes.

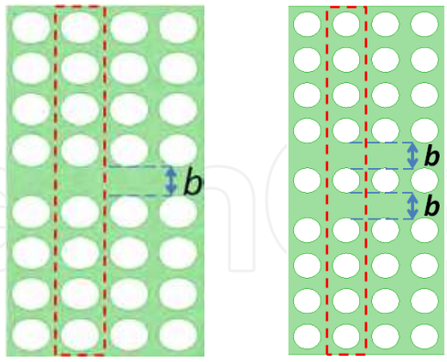

Fig. 11. The definition of square single- (left) and dual-channel (right) air-hole lattices with regions chosen for an FDTD simulation (see red dashed line).

A single simulation of a model consisting of 220 320 FDTD cells (ca. 26MB RAM) takes 140 seconds on Intel Core i7 CPU 950 with the speed of 220 iter/sec. An FDTD cell size is set to $a/20$, leading to at least 40 FDTD cells per wavelength in free space and ca. 12 in the membrane. Thus, calculation of the whole PBG diagram with the step of $\pi/10$ takes about 19 x 140 sec = 45 minutes.

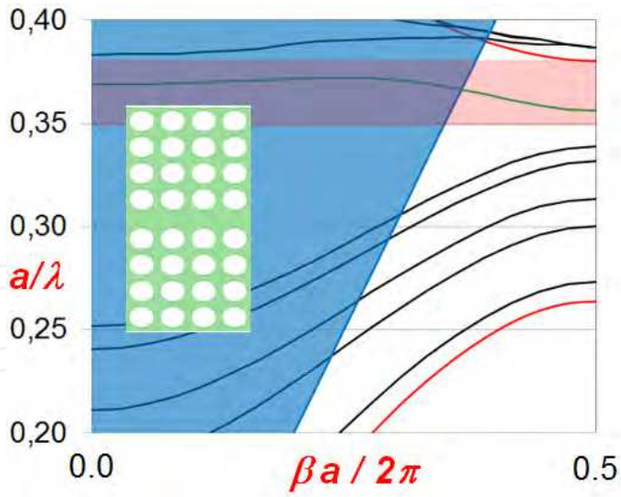

Fig. 12. A TE mode photonic bandgap diagram for a single-channel in an air-hole square lattice cut in an InGaAsP membrane (n = 3.4, r/a = 0.4, d/a = 0.4, b/a = 0.3). The light cone is shown with a blue semi-transparent colour.

Fig.13 shows a PBG diagram for TE polarisation computed for a square dual-channel (n = 3.4, r/a = 0.4, d/a = 0.6, b/a = 0.3). Two supermodes are distinguished with blue and green colours. However, only the 1st order supermode (green) has a uniquely defined phase constant within a photonic bandgap (red semi-transparent zone), additionally reduced by a light cone to the a/λ = 0.337… 0.342 spectrum range (1.5% wide). Comparing the results shown in Fig.14 with those in Fig.13, it can be seen that an increase in the channel's width b/a from 0.3 to 0.4 results in a decrease of the supermode's frequency. Most of the 1st order supermode's unique phase constant range shown in Fig.14 is within the photonic bandgap (red semi-transparent zone). Unfortunately, the light cone limits the choice to the a/λ = 0.318… 0.323 spectrum range (1.5% wide). In this case, however, the allowed spectrum is more distant from the 2nd order supermode (blue), reducing the risk of its unintended oscillation. On the other hand, excitation of the modes in the photonic crystal surrounding the channel is more likely to happen. Concluding, it can be seen that an appropriate adjustment of the light cone, photonic bandgap and channel's width gives a lot of possibilities to modify the allowed supermode's spectrum range (Lesniewska-Matys, 2011).

In the next Section, electric field distributions of a few exemplary supermodes obtained in photonic crystal membrane channels are given.

3.3 Electromagnetic field distribution in photonic crystal membrane channels

The calculation of laser characteristics of above-threshold generation in the considered PhC membrane channels requires quantitative knowledge of a field distribution of an undisturbed travelling wave propagating along the channel at one of selected modes (see Section 4.3). Therefore, envelopes of electric field components within a unit row of the photonic crystal waveguides have to be computed. For that purpose, an FDTD computational model as shown in Fig.15 is used to generate a travelling wave in the channel(s), which may be then integrated in time to obtain the envelopes. The photonic crystal is equipped on the left with an additional input section, where an appropriate mode

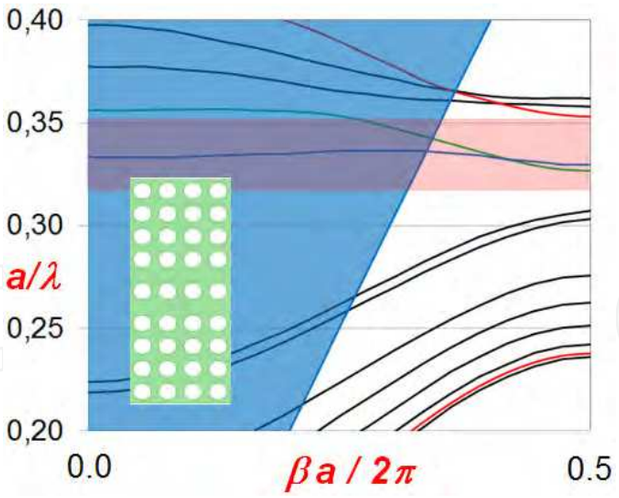

Fig. 13. A TE mode photonic bandgap diagram for a dual-channel in an air-hole square lattice cut in an InGaAsP membrane (n = 3.4, r/a = 0.4, d/a = 0.6, b/a = 0.3). The light cone is shown with a blue semi-transparent colour.

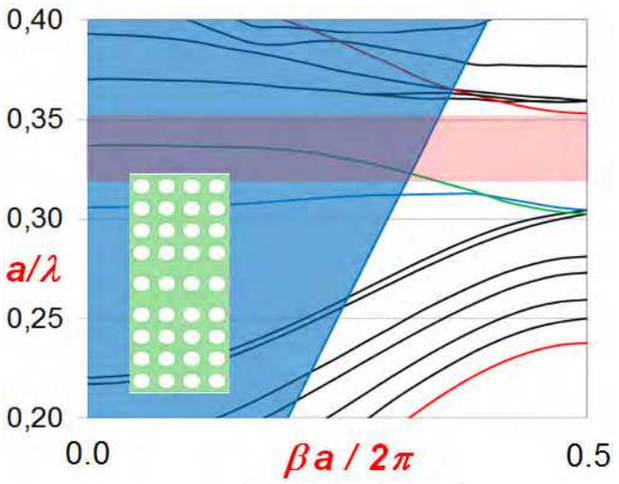

Fig. 14. A TE mode photonic bandgap diagram for a dual-channel in an air-hole square lattice cut in an InGaAsP membrane (n = 3.4, r/a = 0.4, d/a = 0.6, b/a = 0.4). The light cone is shown with a blue semi-transparent colour.

is excited using a mode template generation technique (Celuch-Marcysiak et al., 1996). The end of the waveguide on the right is truncated with a perfectly matched layer (PML) (Berenger, 1994) to avoid any reflections that would disturb the travelling wave.

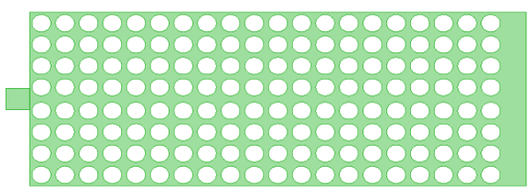

Fig. 15. The view of an FDTD model of a photonic crystal waveguide.

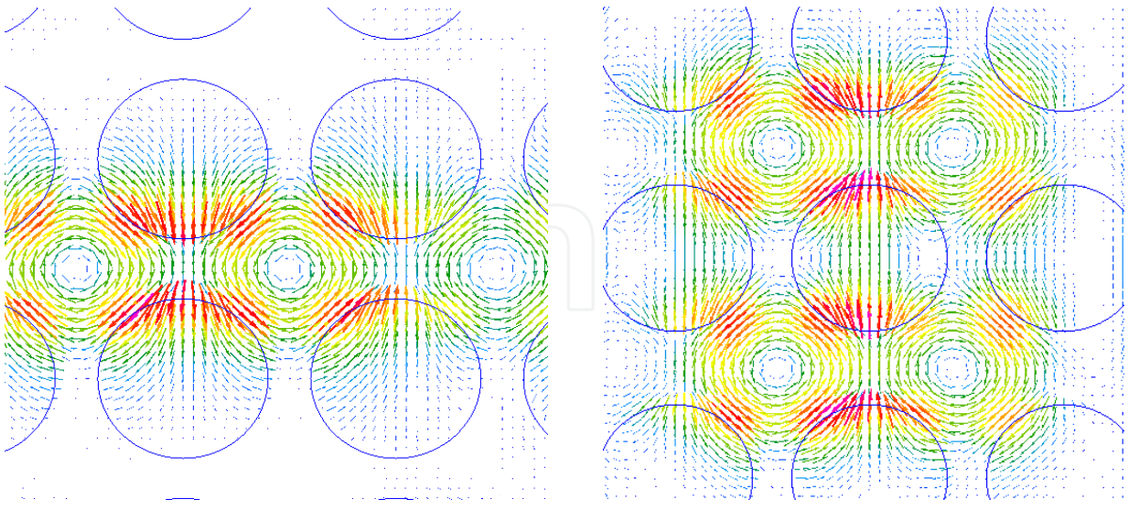

Fig. 16. Vector views of an instantaneous electric field for a/λ = 0.356 (left) and for a/λ = 0.321 (right) for the single-channel (left) and dual-channel (right) waveguides, the PBG diagrams of which are shown in Fig.12 and Fig.14, respectively.

For instance, Fig.16 shows the distribution of an instantaneous electric field vector in the single-channel waveguide for a/λ = 0.356. It can be seen that the field is mostly concentrated within the channel near the hole and has its minimum in the middle between the rows, where the longitudinal electric component dominates over the transverse one. Similarly, Fig.17 presents the distribution of an instantaneous electric field vector in the dual-channel waveguide for a/λ = 0.321. This time, it is crucial to determine whether the fields in both channels oscillate in-phase or not. A thorough look onto the picture reveals that vectors in the adjacent channels have the same direction prompting the conclusion that both modes creating the supermode are in-phase polarised. Thus, the gain of a far-field radiation pattern increases leading to higher laser beam intensity.

Instantaneous electric field distributions like those shown in Fig.16 are, afterwards, integrated in time and in a whole volume of a single row of a channel. As it is shown in the subsequent Section, those envelopes are used to compute gain characteristics of phased array lasers based on photonic crystal membranes.

4. Supermode laser generation in photonic crystal membranes

4.1 The model of an effective planar waveguide

Taking advantage of the already computed PBG diagrams of the photonic crystal membranes with one and two waveguide channels (see Section 3), the phase constant of the supermodes may be easily determined. That knowledge is essential to build an equivalent effective waveguide model, which enables an approximate analytical representation of a field distribution of the guided modes in passive structures (Lesniewska-Matys, 2011). As it can be seen in Fig.17, in the proposed model, a photonic crystal waveguide is replaced with a two dimensional planar one with the same membrane's thickness but the channel's width adjusted so as to obtain the same phase constant.

Refractive indices in the planar equivalent structure are chosen in the following way: the refractive index of a waveguide core (n_1 in Fig.17b) is the same as in the photonic crystal structure, while n_4 and n_5 are equal to the value of the material filling the holes in the photonic crystal structure (air in the examples considered in this Chapter).

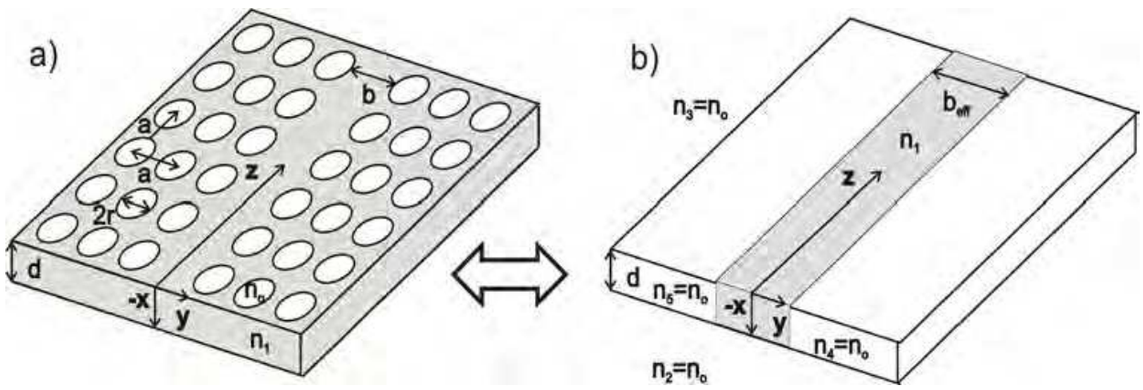

Fig. 17. A perspective view of a) a single-channel in a square-PhC membrane and b) an effective planar waveguide equivalent.

Next, to evaluate the field distribution in the already defined effective planar waveguide, a method proposed in (Marcuse, 1974) is applied. Those analytically derived waveguide modes are used, afterwards, to describe the operation of laser modes in such effective planar waveguides. Subsequently, the field distribution in a multichannel structure with the propagating supermodes is obtained using a non-orthogonal (strongly) coupled mode theory as proposed in (Chuang, 1987a; Chuang, 1987b; Chuang, 1987c). The overlapping integrals between the modes and their coupling coefficients in planar dual-channel waveguides are derived using formulae describing an EM field distribution in the single-channel planar structure. Eventually, the obtained field distributions for the single- and dual-channel structures may be used to estimate approximate operation conditions of laser structures above a generation threshold. (see Section 4.3).

4.2 Mode propagation in an effective N-waveguide structure

Fig.18 shows a top view of a dual-channel defect waveguide, where shaded regions indicate the equivalent effective planar structure. The channels' widths in the equivalent model are adjusted so as to provide the same phase constant of the fundamental supermode as in the corresponding PhC channels.

A total EM field distribution in the coupled planar waveguides may be represented as a weighted sum of the modes propagating in each of the waveguides separately:

$$\vec{E}_t(x,y) = \sum_{p=1}^{N} \vec{a}_p(z)\, \vec{E}_t^{(p)}(x,y) \tag{3}$$

$$\vec{H}_t(x,y) = \sum_{p=1}^{N} \vec{a}_p(z)\, \vec{H}_t^{(p)}(x,y) \tag{4}$$

$$\vec{E}_z(x,y) = \sum_{p=1}^{N} \vec{a}_p(z) \frac{\varepsilon^{(p)}}{\varepsilon} \vec{E}_z^{(p)}(x,y) \tag{5}$$

$$\vec{H}_z(x,y) = \sum_{p=1}^{N} \vec{a}_p(z)\, \vec{H}_z^{(p)}(x,y) \tag{6}$$

where: $\vec{E}_t$, $\vec{H}_t$, ($\vec{E}_z$, $\vec{H}_z$) denote transverse (longitudinal) electric and magnetic field components, respectively.

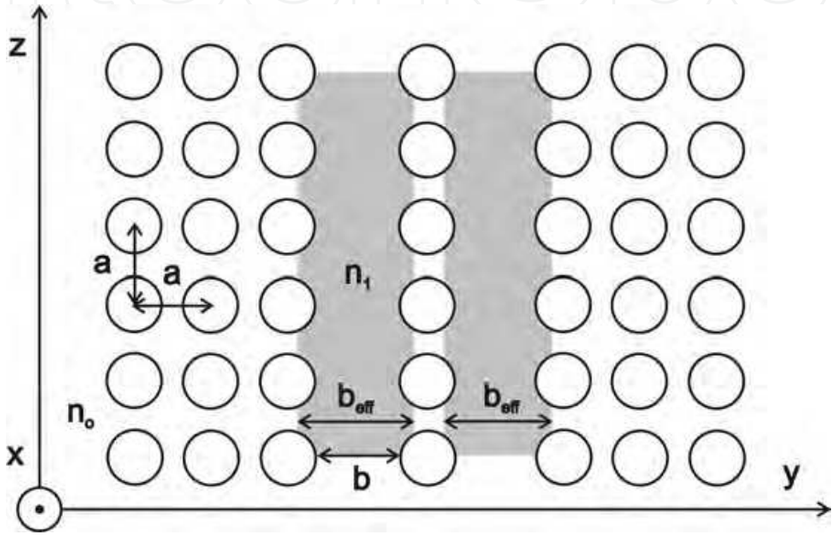

Fig. 18. A top view of a dual-channel defect waveguide processed in a membrane with a photonic crystal square lattice. Shaded regions indicate an equivalent effective waveguide structure.

According to (Kogelnik & Shank, 1972; Schmidt et al., 1974; Chen & Wang, 1984), the amplitudes of the modes guided in the coupled waveguides satisfy the following conditions:

$$\bar{C}\frac{d}{dz}\vec{a}(z) = i\,S\,\vec{a}(z) \quad \text{or} \quad \frac{d}{dz}\vec{a}(z) = i\,M\,\vec{a}(z) \tag{7}$$

where an *N*-element vector $\vec{a}(z)$ consists of $a_p(z)$ amplitudes of the modes propagating in consecutive waveguide channels.

The matrices *S* and *M* are defined as follows:

$$S = \bar{C}B + \tilde{K} \quad \text{or} \quad M = \bar{C}^{-1}S = B + \bar{C}^{-1}\tilde{K} \tag{8}$$

where $\bar{C}$ is an *N*x*N* square matrix, where each element of the overlapping integrals $\bar{C}_{pq}$ is defined as follows:

$$\bar{C}_{pq} = \bar{C}_{qp} = \frac{C_{pq} + C_{qp}}{2} \tag{9}$$

where

$$C_{pq} = \frac{1}{2}\int_{-\infty}^{\infty}\int_{-\infty}^{\infty}\left(\vec{E}_t^{(q)} \times \vec{H}_t^{(p)}\right)\hat{z}\, dx\, dy \tag{10}$$

It should be emphasized that the electromagnetic field was normalised so as to:

$$C_{pp} = C_{qq} = 1 \tag{11}$$

Another *N*x*N* matrix $\tilde{K}$, applied in Eq.8, consists of coupling coefficients between all the *N* waveguides, which are defined in the following way:

$$\tilde{K}_{pq} = \frac{\omega}{4}\int_{-\infty}^{\infty}\int_{-\infty}^{\infty}\Delta\varepsilon^{(q)}\left[\vec{E}_t^{(p)}\cdot\vec{E}_t^{(q)} - \frac{\varepsilon^{(p)}}{\varepsilon}\vec{E}_z^{(p)}\cdot\vec{E}_z^{(q)}\right]dx\, dy \tag{12}$$

where: $\Delta\varepsilon^{(q)} = \varepsilon - \varepsilon^{(q)}$, $\varepsilon^{(q)} = \left(n^{(q)}\right)^2$.

The matrix *B* is an *N*x*N* diagonal matrix with phase constants β_i (i = 1…*N*) of the modes propagating in all the waveguide channels. It should be noted that matrices $\overline{C}$ and *S* are symmetric, what is very important to prove the orthogonality of the supermodes, whereas the matrix *M*, in general, is not necessarily symmetric.

The solution of the coupled mode equations given by Eq.8 leads to the modal field distribution in the entire array for a given propagation constant γ_P. In the system consisting of *N* coupled waveguides, *P* supermodes are generated (*N* = *P*), which may be written as follows:

$$\begin{aligned}
\tilde{E}_1 &= A_1\cdot\left[a_1^{(1)}(z)E_1^{(1)}(x,y) + \ldots + a_N^{(1)}(z)E_N^{(1)}(x,y)\right]\cdot e^{i\gamma_1 z}\\
&\vdots\\
\tilde{E}_P &= A_P\cdot\left[a_1^{(P)}(z)E_1^{(P)}(x,y) + \ldots + a_N^{(P)}(z)E_N^{(P)}(x,y)\right]\cdot e^{i\gamma_P z}
\end{aligned} \tag{13}$$

where A_k (k = 1…*P*) are scaling coefficients, *P* is the order of a supermode, and $a_N^{(1)}$ indicates the amplitude of a field distribution of the 1st supermode in the *N*th waveguide.

4.3 The model of light generation in planar multi-channel photonic crystal membrane lasers

In this Section, an approximate model of laser generation in planar multi-channel PhC membranes is described. Fig.19 shows phased array lasers with mirrors made of 1D and 2D photonic crystals processed in a membrane. The effective values of reflection coefficients are denoted with r_1 and r_2. It is assumed hereafter that the reflection coefficient of an input mirror is r_1 = 1.0.

In the proposed model of light generation, a field distribution in the single- and multi-channel photonic crystal membrane lasers is substituted with a field in the equivalent effective planar waveguides (see Section 4.2). To achieve laser characteristics of those

structures, energy theorem is used (Szczepanski et al., 1989; Szczepanski, 1988). It allows us to represent a normalised small-signal gain saturation of the laser as a function of a saturation power, a distributed losses coefficient and a laser's geometry. The field distribution of the modes generated in the membrane was obtained in two ways: applying the FDTD method (Taflove & Hagness, 2005; QWED) and using analytical formulas derived for the effective planar waveguides. As it is shown in the next Section, discrepancy between lasers characteristics achieved with both methods remains below ca. 10 %.

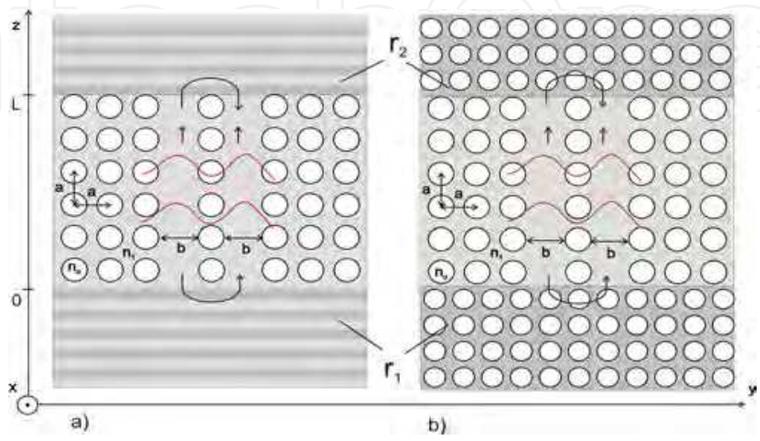

Fig. 19. A schematic view of phased array photonic crystal lasers processed in a membrane with a square photonic crystal lattice with mirrors made of a) a 1D photonic crystal and b) a 2D photonic crystal.

The field distribution in the laser is written in the following way:

$$E(x,y,z) = R(x,y,z) + S(x,y,z) = f_R(z)\,E_R(x,y,z)\,e^{i\beta z} + \\ + f_S(z)\,E_S(x,y,z)\,e^{-i\beta z} \tag{14}$$

where β is a phase constant of a laser mode, $f_R(z)$ and $f_S(z)$ denote complex amplitudes of forward and backward propagating waves, whereas $E_R(x,y,z)$ and $E_S(x,y,z)$ represent a transverse distribution of the laser mode.

The coupled-mode equations for the considered laser structures may be written as (Szczepanski, 1994):

$$\begin{cases} \dfrac{df_R(z)}{dz} + (\alpha_L - i\delta) f_R(z) = \dfrac{1}{N_R}\iint g_o\,\gamma\,D\,d_\alpha\,f_R(z)\left|E_R(x,y,z)\right|^2 dxdy + \\ + \dfrac{1}{2N_R}\iint g_o\,\gamma\,D\,d_\kappa\,f_S(z)\,E_S(x,y,z)\,E_R^*(x,y,z)\,dxdy, \\ -\dfrac{df_S(z)}{dz} + (\alpha_L - i\delta) f_S(z) = \dfrac{1}{N_S}\iint g_o\,\gamma\,D\,d_\alpha\,f_S(z)\left|E_S(x,y,z)\right|^2 dxdy + \\ + \dfrac{1}{2N_S}\iint g_o\,\gamma\,D\,d_\kappa^*\,f_R(z)\,E_R(x,y,z)\,E_S^*(x,y,z)\,dxdy, \end{cases} \tag{15}$$

where g_o is a small-signal gain coefficient, α_L stands for laser's distributed losses, δ denotes a frequency-shift parameter understood as the discrepancy between an oscillating frequency in passive and active resonators. The normalisation factors N_R and N_S may be calculated as:

$$N_R = \iint \left|E_R(x,y,z)\right|^2 dxdy\,,\ N_S = \iint \left|E_S(x,y,z)\right|^2 dxdy \tag{16}$$

The shape of a gain spectral line applied in Eq.15 is given by:

$$D = \left(\gamma + i\left(\omega - \upsilon\right)\right)^{-1} \tag{17}$$

whereas the other parameters are given as follows:

$$C_i = 1 + \left[\left|f_R(z)\,E_R(x,y,z)\right|^2 + \left|f_S(z)\,E_S(x,y,z)\right|^2\right]\cdot\frac{L}{I_S} \tag{18}$$

$$C_c = 2\left[\left|f_R(z)\,E_R(x,y,z)\right|^2 \cdot \left|f_S(z)\,E_S(x,y,z)\right|^2\right]\cdot\frac{L}{I_S} \tag{19}$$

$$d_\alpha = \left(C_i^2 - C_c^2\right)^{-0.5} \tag{20}$$

$$d_\kappa = -C_c\, e^{i\theta}\left[\sqrt{C_i^2 - C_c^2}\left(C_i + \sqrt{C_i^2 - C_c^2}\right)\right]^{-1} \tag{21}$$

where L denotes the length of the laser (see Fig.19).

The saturation power in the active region can be written as:

$$P_S = I_S \cdot A_l \tag{22}$$

where I_S is a saturation intensity

$$I_S = \frac{h\upsilon}{\sigma\tau} \tag{23}$$

and A_l denotes a cross-section of the laser, h is the Planck constant, υ is the frequency of a laser mode, σ is an emission cross-section, τ represents recombination lifetime in the active region.

Operations on Eq.15 lead to (Szczepanski et al., 1989; Szczepanski, 1988):

$$\begin{aligned}
&\frac{d}{dz}\left(\left|f_R(z)\right|^2 - \left|f_S(z)\right|^2\right) = -2\alpha_L\left(\left|f_R(z)\right|^2 + \left|f_S(z)\right|^2\right) + \frac{2L(\omega-\upsilon)}{N^R}\int\frac{g_o\left|f_R(z)\right|^2\left|E^R(x,y,z)\right|^2}{\sqrt{C_i^2 - C_c^2}}dxdy + \\
&+\frac{2L(\omega-\upsilon)}{N^S}\int\frac{g_o\left|f_S(z)\right|^2\left|E^S(x,y,z)\right|^2}{\sqrt{C_i^2 - C_c^2}}dxdy - \frac{2L(\omega-\upsilon)}{N^R}\int\frac{g_o\left|f_S(z)E^S(x,y,z)\right|\left|f_R(z)E^R(x,y,z)\right|}{\sqrt{C_i^2 - C_c^2}\left(C_i + \sqrt{C_i^2 - C_c^2}\right)}dxdy + \\
&-\frac{2L(\omega-\upsilon)}{N^S}\int\frac{g_o\left|f_R(z)E^R(x,y,z)\right|\left|f_S(z)E^S(x,y,z)\right|}{\sqrt{C_i^2 - C_c^2}\left(C_i + \sqrt{C_i^2 - C_c^2}\right)}dxdy.
\end{aligned} \tag{24}$$

The solution of Eq.24 requires boundary conditions to be specified:

$$\left|f_R(0)\right| = r_2\left|f_S(0)\right| \tag{25}$$

$$P_{S,\,out} = \left|f_S(0)\right|^2\left(1-r_2^2\right)\iint\left|E_S(x,y,0)\right|^2 dxdy \tag{26}$$

$$\left|f_S(L)\right| = r_1\left|f_R(L)\right| \tag{27}$$

$$P_{R,\,out} = \left|f_R(L)\right|^2\left(1-r_1^2\right)\iint\left|E^R(x,y,L)\right|^2 dxdy \tag{28}$$

where $P_{out} = P_{R,\,out} + P_{S,\,out}$ is a total power generated by the laser.

In a threshold approximation, $f_R(z)$ and $f_S(z)$ are equal to:

$$f_R(z) = |A|\exp\left(\gamma_f z\right) \tag{29}$$

$$f_S(z) = |A| r_2^{-1}\exp\left(-\gamma_f z\right) \tag{30}$$

where

$$\gamma_f = \frac{1}{2L}\ln\frac{1}{r_1 r_2} \tag{31}$$

An approximate expression relating the normalised small-signal gain coefficient g_oL to the output power and the parameters of the planar laser is given as follows:

$$g_oL = \frac{C\int_{-d}^{0}\int_{0}^{b_{eff}}\left|E_t(x,y,z)\right|^2 dxdy + 2\alpha_L\int_{-d}^{0}\int_{0}^{b_{eff}}\int_{0}^{L}\left|E_t(x,y,z)\right|^2\cdot\left(\left|f_R(z)\right|^2+\left|f_S(z)\right|^2\right)dxdydz}{2\int_{-d}^{0}\int_{0}^{b_{eff}}\int_{0}^{L}\frac{\left|E_t(x,y,z)\right|^2\cdot\left(\left|f_R(z)\right|^2+\left|f_S(z)\right|^2\right)}{1+\frac{P_{out}}{P_S}\frac{1}{K}\left|E_t(x,y,z)\right|^2\cdot\left(\left|f_R(z)\right|^2+\left|f_S(z)\right|^2\right)}dxdydz}, \tag{32}$$

where:

$$K = \left|f_R(L)\right|^2\left(1-r_1^2\right)+\left|f_S(0)\right|^2\left(1-r_2^2\right) \tag{33}$$

The transverse electric field distribution of the laser mode in the photonic crystal membrane $E_R = E_S = E_t$ was calculated numerically (see Section 3.3) and analytically using the effective planar waveguide model (see Section 4.2).

4.4 Laser gain characteristics

In this Section, exemplary gain characteristics of phased array lasers processed in defect photonic crystal membranes are given. The transverse field distribution of the

laser supermode is calculated numerically with the FDTD method (Taflove & Hagness, 2005; QWED) and analytically, using the non-orthogonal mode theory applied to the calculation of the effective waveguide structure. It is assumed that the distributed losses coefficient is equal to α_L = 200 cm^{-1} (Zielinski et al. 1989; Lu et al., 2008), whereas the output power to saturation power ratio is $P_{out} / P_s = 10^{-6}$ (Lu et al., 2009; Susaki et al., 2008; van den Hoven, 1996).

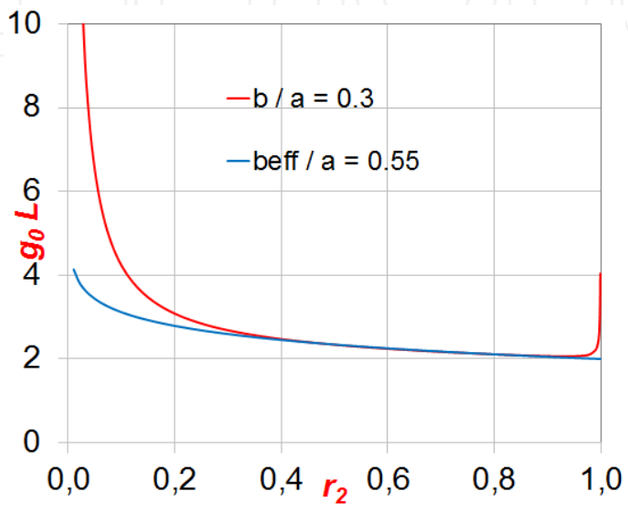

Fig. 20. A normalised small-signal gain at $\lambda = 1.55\mu m$ as a function of cavity mirror reflectivity for a single-channel square-PhC membrane laser (r/a = 0.4, d/a = 0.4, b/a = 0.3, $a = 0.55\mu m$). Red curve: computed with the aid of FDTD for (a/λ , βa) = (0.356, π); blue curve: effective waveguide model with b_{eff} / a = 0.55.

Fig.20 presents a normalised small-signal gain at $\lambda = 1.55\mu m$ as a function of output mirror reflectivity r_2 for a single-channel square-PhC membrane laser (r/a = 0.4, d/a = 0.4, b/a = 0.3, $a = 0.55\mu m$), the PBG diagram of which is shown in Fig.12. The red curve depicts the gain characteristics calculated for (a/λ , βa) = (0.356, π) with the aid of FDTD, whereas the blue one indicates the result of analytical computation with Eq.32 for the corresponding effective waveguide model with the channel width b_{eff} / a = 0.55. In principle, the minimum of the calculated characteristics indicates an optimum value of the mirror reflection coefficient r_2 of an output mirror, for which maximum output power efficiency is achieved. It can be seen from Fig.20 that, although the shape of both curves is substantially different, their minima are in a similar position and the optimum reflectivity r_2 amounts to 0.93 and 0.997 for the red and blue curves, respectively. Consequently, it leads to ca. 7.2% of a relative discrepancy between the optimum values computed with the two approaches.

Similar computations were carried out for dual-channel scenarios with r/a = 0.4, d/a = 0.6, b/a = 0.3 and 0.4. Fig.21,22 show the corresponding laser characteristics for (a/λ, βa) = (0.340, 13π/18) and (0.321, 12π/18) with $a = 0.53\mu m$ and $0.50\mu m$, respectively. In both cases, the

reflection coefficient r_2 is equal to 0.91 and 0.996 for numerical and analytical (effective) computations, respectively, leading to ca. 9.4% of the relative discrepancy.

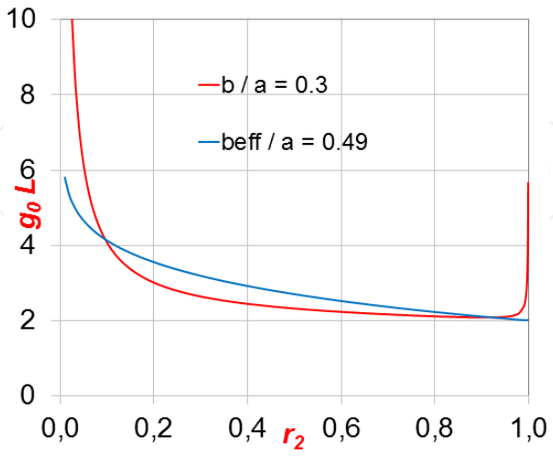

Fig. 21. A normalised small-signal gain at $\lambda = 1.55\mu m$ as a function of cavity mirror reflectivity for a single-channel square-PhC membrane laser ($r/a = 0.4$, $d/a = 0.6$, $b/a = 0.3$, $a = 0.53\mu m$). Red curve: computed with the aid of FDTD for $(a/\lambda\ ,\ \beta a) = (0.340,\ 13\pi/18)$; blue curve: effective waveguide model with $b_{eff}/a = 0.49$.

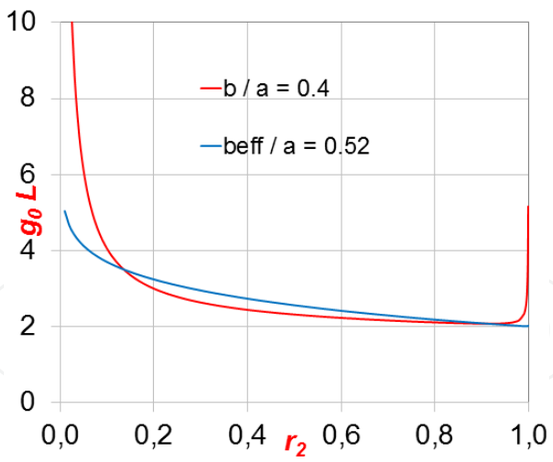

Fig. 22. A normalised small-signal gain at $\lambda = 1.55\mu m$ as a function of cavity mirror reflectivity for a single-channel square-PhC membrane laser ($r/a = 0.4$, $d/a = 0.6$, $b/a = 0.4$, $a = 0.50\mu m$). Red curve: computed with the aid of FDTD for $(a/\lambda\ ,\ \beta a) = (0.321,\ 12\pi/18)$; blue curve: effective waveguide model with $b_{eff}/a = 0.52$.

Concluding, exemplary laser small-signal gain characteristics have been shown, which enable the generation of a laser single-mode both in the single- and dual-channel structures

in two-dimensional photonic crystal lattices processed in dielectric membranes. It has also been shown that both rigid full-wave and approximate computations of the modal field distributions provide the values of the optimum reflection coefficient of the output mirror, which are in less than 10% agreement.

5. Conclusions

In this Chapter, a complete design cycle of phased array lasers based on photonic crystals processed in dielectric membranes has been given. First, full-wave electromagnetic computations with the FDTD method allow us to determine a photonic bandgap of the selected passive photonic crystal lattices processed in a dielectric membrane. Second, a single- either multi-channel waveguide array is introduced into the lattice and dispersive properties of the modes within the corresponding photonic bandgap are computed. The goal is to evaluate the spectrum, where a single-mode propagation of the supermodes is possible along the channels. Third, for given geometry settings and the mode's wavelength spectrum, the above-threshold laser small-signal gain characteristic is computed with the non-orthogonal coupled mode theory. Gain computations are two-fold. In the first approach, numerical computations of an electric field envelope within a passive structure are executed with the aid of the FDTD method, while the second method is based on an equivalent effective waveguide structure. Both methods provide similar values of the optimum reflection coefficient of the output mirror.

6. References

AcMey, D.E. & Engelmann, R.W.H., High power leaky mode multiple stripe laser, *Appl. Phys. Lett.*, vol. 39, no. 7, pp. 27-29, 1981

Berenger, J.P., A perfectly matched layer for the absorption of electromagnetic waves, *J. Comput. Phys.*, vol. 114, no. 2, pp. 185-200, 1994

Celuch-Marcysiak, M. & Gwarek, W.K., Spatially looped algorithms for time-domain analysis of periodic structures, *IEEE Trans. Microwave Theory Tech.*, vol. MTT-43, No. 4, pp. 860-865, 1995

Celuch-Marcysiak, M., Kozak, A. & Gwarek, W.K., A new efficient excitation scheme for the FDTD method based on the field and impedance template, *IEEE Antennas and Propag. Symp.*, Baltimore, 1996

Chen, K.-L. & Wang, S., Cross-talk problems in optical directional couplers, *Appl. Phys. Lett.*, vol. 44, no. 2, pp. 166-168, 1984

Chow, E., Lin, S.Y., Wendt, J.R., Johnson, S.G. & Joannopoulos, J.D., Quantitative analysis of bending efficiency in photonic-crystal waveguide bends at λ=1.55μm wavelengths, *Optics Letters*, vol. 26, no. 5, pp. 286-288, 2001

Chuang, S.-L., A coupled mode formulation by reciprocity and a variational principle, *J. Lightwave. Technol.*, vol. 5, no. 1, pp. 5-15, 1987

Chuang, S.-L., A coupled mode theory for multiwaveguide systems satisfying the reciprocity theorem and power conservation, *J. Lightwave. Technol.*, vol. 5, no. 1, pp. 174-183, 1987

Chuang, S.-L., Application of the strongly coupled mode theory to integrated optical devices, *J. Quant. Electron*., vol. 23, no. 5, pp. 499-509, 1987

Collin, R.E., *Field Theory of Guided Waves*, McGraw-Hill Inc., New York, 1960

Digonnet, M.J.F. & Shaw, H.J., Analysis of a tunable single mode optical fiber coupler, *J. Quant. Electron*., vol. 18, no. 4, pp. 746-754, 1982

Fan, S., Villeneuve, P.R. & Joannopoulos, J.D., Channel drop filters in photonic crystals, *Optics Letters*, vol. 3, no. 1, pp. 4-11, 1998

Gwarek, W.K., Analysis of an arbitrarily-shaped planar circuit - a time-domain approach, *IEEE Trans. Microwave Theory Tech.*, vol. MTT-33, No.10, pp.1067-1072, 1985

Gwarek, W.K., Morawski, T. & Mroczkowski, C., Application of the FDTD Method to the Analysis of the Circuits Described by the Two-Dimensional Vector Wave Equation, *IEEE Trans. Microwave Theory Tech.*, vol. 41, no. 2, pp. 311-316, Feb. 1993

Hardy, A. & Streifer, W., Coupled mode theory of parallel waveguides, *J. Lightwave Technol.*, vol. 3, no. 5, pp. 1135-1146, 1985

Hardy, A., Streifer, W. & Osinski, M., Chirping effects in phase-coupled laser arrays, *Proc. IEEE*, vol. 135, no. 6, pp. 443-450, 1988

Joannopoulos, J.D., Johnson, S.G., Winn, J.N. & Meade, R.D., *Photonic Crystals. Molding the flow of light*, Second Edition, Princeton University Press, ch. 8, pp. 144, 2008

Kapon, E., Lindsey, P., Katz, J., Margalit, S. & Yariv, A., Chirped arrays of diode lasers for supermode control, *Appl. Phys. Lett.*, vol. 45, no. 3, pp. 200-202, 1984

Kapon, E., Lindsey, P., Smith, J.S., Margalit, S. & Yariv, A., Inverted-V chirped phased arrays of gain-guided GaAs/GaAlAs diode lasers, *Appl. Phys. Lett.*, vol. 45, no. 12, pp. 1257-1259, 1984

Kapon, E., Katz, J., Margalit, S. & Yariv, A., Controlled fundamental supermode operation of phase-locked arrays of gain-guided diode lasers, *Appl. Phys. Lett.*, vol. 45, no. 6, pp. 600-602, 1984

Kapon, E., Rav-Noy, Z., Margalit, S. & Yariv, A., Phase-Locked Arrays of Buried-Ridge InP/InGaAsP Diode Lasers, *J. Lightwave Technol.*, vol. 4, no. 7, pp. 919-925, 1986

Kogelnik, H. & Shank, C.V., Coupled-wave theory of distributed feedback lasers, *J. Appl. Phys.*, vol. 43, no. 5, pp. 2327-2335, 1972

Kogelnik, H. & Schmidt, R.V., Switched directional couplers with alternating Δβ", *J. Quant. Electron.*, vol. 12, no. 7, pp. 396-401, 1976

Kogelnik, H., *Theory of dielectric waveguides*, ch. 2, T.Tamir Edition, New York: Springer-Verlag, 1979

Lesniewska-Matys, K., *Modelowanie generacji promieniowania w planarnym wielokanałowym laserze sprzężonym fazowo zbudowanym na bazie dwuwymiarowego kryształu fotonicznego,* Ph.D. Thesis, Warsaw University of Technology, 2011

Liu, T., Zakharian, A.R., Fallahi, M., Moloney, J.V. & Mansuripur, M., Multimode Interference-Based Photonic Crystal Waveguide Power Splitter, *J. Lightwave Technol.*, vol. 22, no. 12, pp. 2842-2846, 2004

Loncar, M., Doll, T., Vuckovic, J. & Scherer, A., Design and Fabrication of Silicon Photonic Crystal Optical Waveguides, *J. Lightwave Technol.*, vol. 18, no. 10, pp. 1402-1411, 2000

Lu, L., Mock, A., Bagheri, M., Hwang, E.H., O'Brien, J. & Dapkus, P.D., Double-heterostructure photonic crystal lasers with lower thresholds and higher slope efficiencies obtained by quantum well intermixing, *Opt. Express*, vol. 16, no. 22, pp. 17342-17347, 2008

Lu, L., Mock, A., Yang, T., Shih, M.H., Hwang, E.H., Bagheri, M., Stapleton, A., Farrell, S., O'Brien, J. & Dapkus, P.D., 120μW peak output power from edge-emitting photonic crystal doubleheterostructure nanocavity lasers, *Appl. Phys. Lett.*, vol. 94, pp. 111101, 2009

Marcuse, D., *Theory of dielectric optical waveguides*, ch. 1.7, Academic Press, New York and London, 1974

Massaro, A., Errico, V., Stomeo, T., Cingolani, R., Salhi, A., Passaseo, A. & De Vittorio, M., 3-D FEM Modeling and Fabrication of Circular Photonic Crystal Microcavity, *J. Lightwave. Technol.*, vol. 26, no. 16, pp. 2960-2968, 2008

Mei, K.K. & Fana, J., Superabsorption - A Method to Improve Absorbing Boundary Conditions, *IEEE Trans. Antennas & Propagat.*, vol. AP-40, pp. 1001-1010, 1992

Mukai, S., Lindsey, C., Katz, J., Kapon, E., Rav-Noy, Z., Margalit, S. & Yariv, A., Fundamental mode oscillation of a buried ridge waveguide laser array, *Appl. Phys. Lett.*, vol. 45, no. 8, pp. 834-835, 1984

Park, I., Lee, H-S., Kim, H-J., Moon, K-M., Lee, S-G., O, B-H., Park, S-G. & Lee, E-H., Photonic crystal power-splitter based on directional coupling, *Opt. Express*, vol. 12, no. 15, pp. 3599-3604, 2004

QuickWave-3D, QWED Sp. z o.o. Available: http://www.qwed.com.pl

Ren, C., Tian, J., Feng, S., Tao, H., Liu, Y., Ren, K., Li, Z., Cheng, B. & Zhang, D., High resolution three-port filter in two dimensional photonic crystal slabs, *Optics Letters*, vol. 12, no. 21, pp. 10014-10020, 2006

Salski, B., *Application of semi-analytical algorithms in the finite-difference time-domain modeling of electromagnetic radiation and scattering problems*, Ph.D. Thesis, Institute of Radioelectronics, Warsaw University of Technology, 2010

Schmidt, R.V., Flanders, D.C., Shank, C.V. & Standley, R.D., Narrow-band grating filters for thin-film optical waveguides, *Appl. Phys. Lett.*, vol. 25, no. 11, pp. 651-652, 1974

Scifres, D.R., Streifer, W. & Burnham, R.D., Experimental and analytic studies of coupled multiple stripecdiode lasers, *J.Quant. Electron.*, vol. 15, no. 9, pp. 917-922, 1979

Shih, M.H., Kuang, W., Mock, A., Bagheri, M., Hwang, E.H., O'Brien, J.D. & Dapkus, P.D., High-quality factor photonic crystal heterostructure laser, *Appl. Phys. Lett.*, vol. 89, pp. 101104, 2006

Srinivasan, K., Painter, O., Colombelli, R., Gmachl, C., Tennant, D.M., Sergent, A.M., Sivco, D.L., Cho, A.Y., Troccoli, M. & Capasso, F., Lasing mode pattern of a quantum cascade photonic crystal surface-emitting microcavity laser, *Appl. Phys. Lett.*, vol. 84, no. 21, pp. 4164-4166, 2004

Susaki, W., Kakuda, S., Tanaka, M., Nishimura, H. & Tomioka, A., Influence of Band Offsets on Carrier Overflow and Recombination Lifetime in Quantum Well Lasers Grown on GaAs and InP, *20th International Conference on Indium Phosphide and Related Materials*, France, 2008

Szczepanski, P., Sikorski, D. & Wolinski, W., Nonlinear operation of a planar distributed feedback laser: energy approach, *J. Quant. Electron.*, vol. 25, no. 5, pp. 871-877, 1989

Szczepanski , P., Semiclassical theory of multimode operation of a distributed feedback laser, *J. Quant. Electron.*, vol. 24, no. 7, pp. 1248-1257, 1988

Szczepanski, P., *Rola przestrzennego rozkładu pola w generacji promieniowania w laserze,* Postdoctoral Thesis, Warsaw University of Technology, 1994

Taflove, A. & Hagness, S.C., *Computational Electrodynamics: The Finite-Difference Time-Domain Method*, Artech House Publishers, 2005

Tanaka, Y., Nakamura, H., Sugimoto, Y., Ikeda, N., Asakawa, K. & Inoue, K., Coupling properties in a 2-D photonic crystal slab directional coupler with a triangular lattice of air holes, *J. Quant. Electron.*, vol. 41, no. 1, pp. 76-84, 2005

Taylor, H.F., Optical switching and modulation in parallel dielectric waveguides, *J. Appl. Phys.*, vol. 44, no. 7, pp. 3257-3262, 1973

van den Hoven, G.N., Koper, R.J.I.M., Polman, A., van Dam, C., van Uffelen, J.W.M. & Smit, M.K., Net optical gain at 1.53 mm in Er-doped Al_2O_3 waveguides on silicon, *Appl. Phys. Lett.*, vol. 68, no. 14, pp. 1886-1888, 1996

van der Ziel, J.P., Mikulyak, R.M., Temkin, H., Logan, R.A. & Dupuis, W.D., Optical beam characteristics of Schottky barrier confined arrays of phase-coupled multiquantum well GaAs lasers, *J. Quant. Electron.*, vol. 20, no. 10, pp. 1259-1266, 1984

Vecchi, G., Raineri, F., Sagnes, I., Yacomotti, A., Monnier, P., Karle, T.J., Lee, K-H., Braive, R., Le Gratiet, L., Guilet, S., Beaudoin, G., Talneau, A., Bouchoule, S., Levenson, A. & Raj, R., Continuous-wave operation of photonic bandedge laser near 1.55 μm on silicon wafer, *Opt. Express*, vol. 15, no. 12, pp. 7551-7556, 2007

Yamamoto, N., Watanabe, Y. & Komori, K., Design of photonic crystal directional coupler with high extinction ratio and small coupling length, *Jpn. J. Appl. Phys.*, vol. 44, no. 4B, pp. 2575-2578, 2005

Yang, T., Lipson, S., O'Brien, J.D. & Deppe, D.G., InAs Quantum Dot Photonic Crystal Lasers and Their Temperature Dependence, *Photon. Technol. Lett.*, vol. 17, no. 11, pp. 2244-2246, 2005

Yang, T., Mock, A. & O'Brien, J.D., Edge-emitting photonic crystal double heterostructure nanocavity lasers with InAs quantum dot active material, *Opt. Lett.*, vol. 32, no. 9, pp. 1153-1155, 2007

Yariv, A., Coupled mode theory for guided-wave optics, *J. Quantum Electron.*, vol. QE-9, no. 9, pp. 919-933, 1973

Yariv, A. & Taylor, H. F., Guided-wave optics, *Proc. IEEE*, vol. 62, no. 8, pp. 131-134, 1981

Yariv, A., *Optical Electronics in Modern Communications*, Ch. 13, Oxford University Press, 1997

Zhang, M. & Garmire, E., Single-mode fiber-film directional coupler, *J. Lightwave Technol.*, vol. 5, no. 2, pp. 260-267, 1987

Zielinski, E., Keppler, F., Hausser, S., Pilkuhn, M.H., Sauer, R. & Tsang, W.T., Optical Gain and Loss Processes in GaInAs/InP MQW Laser Structures, *J. Quant. Electron.*, vol. 25, no. 6, pp. 1407-1416, 1989

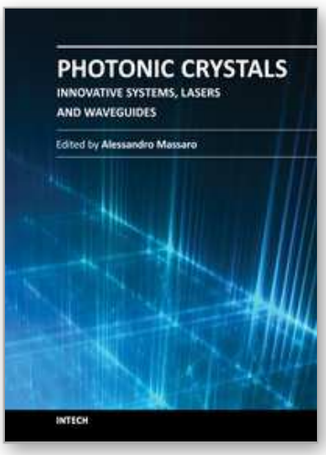

Photonic Crystals - Innovative Systems, Lasers and Waveguides

Edited by Dr. Alessandro Massaro

ISBN 978-953-51-0416-2
Hard cover, 348 pages
Publisher InTech
Published online 30, March, 2012
Published in print edition March, 2012

The second volume of the book concerns the characterization approach of photonic crystals, photonic crystal lasers, photonic crystal waveguides and plasmonics including the introduction of innovative systems and materials. Photonic crystal materials promises to enable all-optical computer circuits and could also be used to make ultra low-power light sources. Researchers have studied lasers from microscopic cavities in photonic crystals that act as reflectors to intensify the collisions between photons and atoms that lead to lazing, but these lasers have been optically-pumped, meaning they are driven by other lasers. Moreover, the physical principles behind the phenomenon of slow light in photonic crystal waveguides, as well as their practical limitations, are discussed. This includes the nature of slow light propagation, its bandwidth limitation, coupling of modes and particular kind terminating photonic crystals with metal surfaces allowing to propagate in surface plasmon-polariton waves. The goal of the second volume is to provide an overview about the listed issues.

INTECH
open science | open minds

InTech Europe
University Campus STeP Ri
Slavka Krautzeka 83/A
51000 Rijeka, Croatia
Phone: +385 (51) 770 447
Fax: +385 (51) 686 166
www.intechopen.com

InTech China
Unit 405, Office Block, Hotel Equatorial Shanghai
No.65, Yan An Road (West), Shanghai, 200040, China
中国上海市延安西路65号上海国际贵都大饭店办公楼405单元
Phone: +86-21-62489820
Fax: +86-21-62489821

IntechOpen